Microscopic optical potentials for calcium isotopes

J. Rotureau,[1] P. Danielewicz,[1,2] G. Hagen,[3,4] G. R. Jansen,[5,3] and F. M. Nunes[1,2]
[1]*NSCL/FRIB Laboratory, Michigan State University, East Lansing, Michigan 48824, USA*
[2]*Department of Physics and Astronomy, Michigan State University, East Lansing, Michigan 48824-1321, USA*
[3]*Physics Division, Oak Ridge National Laboratory, Oak Ridge, Tennessee 37831, USA*
[4]*Department of Physics and Astronomy, University of Tennessee, Knoxville, Tennessee 37996, USA*
[5]*National Center for Computational Sciences, Oak Ridge National Laboratory, Oak Ridge, Tennessee 37831, USA*

(Received 13 August 2018; published 29 October 2018)

We construct nucleonic microscopic optical potentials by combining the Green's function approach with the coupled-cluster method for ^{40}Ca and ^{48}Ca. For the computation of the ground states of ^{40}Ca and ^{48}Ca, we use the coupled-cluster method in the singles-and-doubles approximation, while for the $A = \pm 1$ nuclei we use particle-attached and particle-removed equation-of-motion method truncated at two-particle–one-hole and one-particle–two-hole excitations, respectively. Our calculations are based on the chiral nucleon-nucleon and three-nucleon interaction NNLO$_{\rm sat}$, which reproduces the charge radii of ^{40}Ca and ^{48}Ca, and the chiral nucleon-nucleon interaction NNLO$_{\rm opt}$. In all cases considered here, we observe that the overall form of the neutron scattering cross section is reproduced for both interactions, but the imaginary part of the potential, which reflects the loss of flux in the elastic channel, is negligible. The latter points to neglected many-body correlations that would appear beyond the coupled-cluster truncation level considered in this work. We show that, by artificially increasing the parameter η in the Green's function, practical results can be further improved.

DOI: 10.1103/PhysRevC.98.044625

I. INTRODUCTION

Nuclear reactions are the primary experimental tool to study atomic nuclei. With the recent progress in the development of rare-isotopes beams (RIBs), regions of the nuclear chart far from stability, that were previously out of reach, are now becoming accessible. More progress is expected, with future projects at RIB facilities, to explore systems far from stability [1–3]. In parallel to the progress on the experimental side, efforts should be pursued on the theoretical front to develop or extend reaction models to nuclei far from stability.

It is customary in reaction theory to reduce the many-body picture to a few-body one where only the most relevant degrees of freedom are retained [4]. In that case, one introduces effective interactions, the so-called optical potentials, between the clusters considered. Traditionally, these interactions have been constrained by data, particularly data on stable isotopes. Consequently, the use of these potentials to study exotic nuclei is unreliable and has uncontrolled uncertainties. In order to advance the field of nuclear reactions, it is then critical to connect the effective interaction to an underlying microscopic theory, so that extrapolations to exotic regions are better under control, together with rigorous assessment of uncertainties.

Realistic *ab initio* nuclear structure calculations based on nucleon-nucleon (NN) and three-nucleon forces (3NFs) from chiral effective field theory [5–7] have now reached the point where reliable predictions for nuclei as heavy as ^{100}Sn [8] can be made. This progress is due to the development of many-body methods that scale polynomially with system's size [9–19] and ever-increasing computational power. On the other hand, the *ab initio* nuclear reaction community is behind in reached mass number, precision, and accuracy. There has been a lot of effort in developing microscopic reaction theories for light nuclei starting from realistic NN and 3NFs [20–30], while less so for medium-mass and heavy nuclei [31–35]. With upcoming experiments on rare isotopes in the medium- and heavy-mass regions of the nuclear chart, it is important to develop *ab initio* reaction theory that can make accurate predictions in these mass regions. It is the aim of this paper to take the first steps toward this goal.

In this paper, we will present *ab initio* calculations of nucleon-nucleus optical potential for the doubly magic nuclei ^{40}Ca and ^{48}Ca. This work follows up on a previous study [35]. The optical potential (also known as the self-energy) enters the Dyson equation together with the one-body Green's function. Assuming some approximations for the self-energy, the standard way of obtaining the optical potential is to iterate the nonlinear Dyson equation until a self-consistent solution is obtained. This is known as the self-consistent Green's function approach [11,36–38]. Our approach differs from the self-consistent Green's function approach in that the optical potential is obtained directly by inverting the Dyson equation [35]. We calculate the single-particle Green's function by combining the coupled-cluster method [9,10,39–43] with the Lanczos continued fraction method [27,32,35,44–46] and employing a complex Berggren basis [47–51]. In this work, we focus on the chiral NN and NNN interaction NNLO$_{\rm sat}$, which has been shown to produce accurate ground-state energies and charge radii from light- to medium-mass nuclei [52–56].

This paper is organized as follows. In Sec. II, we briefly revisit the formalism of the Green's function and the

coupled-cluster method along with the Berggren basis. We start Sec. III by showing the convergence pattern of the optical potentials associated with the bound states in ^{41}Ca and ^{49}Ca and then present cross-section results for the neutron elastic scattering on ^{40}Ca and ^{48}Ca. For comparison, we also show calculated elastic cross sections obtained with the NNLO$_{\rm opt}$ [57] interaction (also derived within the chiral-EFT approach) and the phenomenological Koning-Delaroche (KD) potential [58]. Finally, we conclude and discuss future possible applications in Sec. IV.

II. FORMALISM

A. The single-particle Green's function

Let us consider a nucleus with A nucleons. As outlined in Ref. [35], the single-particle Green's function for that nucleus has matrix elements

$$G(\alpha,\beta,E) = \langle\Psi_0|a_\alpha \frac{1}{E-\left(H-E^A_{gs}\right)+i\eta}a^\dagger_\beta|\Psi_0\rangle + \langle\Psi_0|a^\dagger_\beta \frac{1}{E-\left(E^A_{gs}-H\right)-i\eta}a_\alpha|\Psi_0\rangle, \quad (1)$$

where α and β represent single-particle states, and $|\Psi_0\rangle$ represents the ground state of the nucleus with energy E^A_{gs}. By definition, the parameter η is such that in the physical limit $\eta \to 0^+$. The operators $a^\dagger_\alpha$ and a_β create and annihilate a nucleon in the single-particle states α and β, respectively, and their labels are shorthand for the quantum numbers $\alpha = (n, l, j, j_z, \tau_z)$. Here, n, l, j, j_z, τ_z label the radial quantum number, the orbital angular momentum, the total orbital momentum, its projection on the z axis, and the isospin projection, respectively. The intrinsic Hamiltonian H reads

$$H = \sum_{i=1}^{A}\frac{\vec{p}_i{}^2}{2m} - \frac{\vec{P}^2}{2mA} + \sum_{i<j}V_{ij} + \sum_{i<j<k}V_{ijk}, \quad (2)$$

with $\vec{p}_i$ being the momentum of the nucleon i of mass m and $\vec{P} = \sum_{i=1}^{A}\vec{p}_i$ being the momentum associated with the center-of-mass motion. The terms V_{ij} and V_{ijk} are NN and 3NFs, respectively. It is useful to rewrite the Hamiltonian as

$$H = \sum_{i=1}^{A}\frac{\vec{p}_i^2}{2m}\left(1-\frac{1}{A}\right) + \sum_{i<j}\left(V_{ij} - \frac{\vec{p}_i\vec{p}_j}{mA}\right) + \sum_{i<j<k}V_{ijk}, \quad (3)$$

where one separates the one-body and two-body (three-body) contributions. In the following, we work with the single-particle basis solutions of the Hartree-Fock (HF) potential generated by H. We recall here that the HF basis is a good starting point for coupled-cluster calculations and that the HF Green's function denoted as $G^{(0)}$ is a first-order approximation to the Green's function (1). The Green's function fulfills the Dyson equation

$$G(\alpha,\beta,E) = G^{(0)}(\alpha,\beta,E) + \sum_{\gamma,\delta}G^{(0)}(\alpha,\gamma,E) \times \Sigma^*(\gamma,\delta,E)G(\delta,\beta,E). \quad (4)$$

Here, $\Sigma^*(\gamma,\delta,E)$ is the self-energy, which can be obtained from the inversion of Eq. (4):

$$\Sigma^*(E) = [G^{(0)}(E)]^{-1} - G^{-1}(E). \quad (5)$$

Finally, one obtains the optical potential as

$$\Sigma' \equiv \Sigma^* + U, \quad (6)$$

where U is the HF potential. For $E \geqslant E^A_{gs}$, Σ' in Eq. (6) corresponds to the optical potential for the elastic scattering from the A-nucleon ground state [59,60]. For $E \leqslant E^A_{gs}$, Σ' has a discrete number of solutions which correspond to the bound states in the $A+1$ nucleon system. The optical potential is nonlocal, energy-dependent, and complex [60]; for $E \geqslant E^A_{gs}$, its imaginary component describes, by construction, the loss of flux due to absorption into channels other than the elastic channel.

In this paper, the optical potential is obtained by inverting the Dyson equation (4) after a direct computation of the Green's function (1) with the coupled-cluster method [43]. In the following, we present the main steps involved in the computation of the Green's function in our approach.

B. Coupled-cluster approach for the Green's function

In this section, we briefly show how we construct the Green's function following the coupled-cluster method. For a more detailed account, we refer the reader to Refs. [35,41,43]. In coupled-cluster theory, the ground state is represented as

$$|\Psi_0\rangle = e^T|\Phi_0\rangle, \quad (7)$$

where T denotes the cluster operator which gets expanded in the number of particle-hole excitations

$$T = T_1 + T_2 + \cdots = \sum_{i,a}t_i^a a_a^\dagger a_i + \frac{1}{4}\sum_{ijab}t_{ij}^{ab}t_{ijab}a_a^\dagger a_b^\dagger a_j a_i + \cdots. \quad (8)$$

The operators T_1 and T_2 induce 1p-1h and 2p-2h excitations of the HF reference, respectively. Here, the single-particle states $i, j, \ldots$ refer to hole states occupied in the reference state $|\Phi_0\rangle$ while $a, b, \ldots$ denote valence states above the reference state. In practice, the expansion (8) is truncated. In the coupled cluster with singles and doubles (CCSD), all operators T_i beyond $i = 2$ are neglected.

One can show that the CCSD ground state is an eigenstate of the similarity-transformed Hamiltonian $\overline{H} \equiv e^{-T}He^T$ in the space of 0p-0h, 1p-1h, and 2p-2h configurations. Note that the transformed Hamiltonian is not Hermitian because the operator e^T is not unitary. As a consequence, $\overline{H}$ has left and right eigenvectors which constitute a biorthogonal basis with the following completeness relation

$$\sum_i |\Phi_{i,R}\rangle\langle\Phi_{i,L}| = \hat{1}, \quad (9)$$

where the right ground state $|\Phi_{0,R}\rangle$ is the reference state $|\Phi_0\rangle$, while the left ground state is given by $\langle\Phi_{0,L}| = \langle\Phi_0|(1+\Lambda)$ with Λ a linear combination of particle-hole de-excitation operators.

Using the ground state of the similarity-transformed Hamiltonian $\overline{H}$, we can now write the coupled-cluster Green's function G^{CC} as

$$G^{CC}(\alpha,\beta,E) \equiv \langle\Phi_{0,L}|\overline{a_\alpha}\frac{1}{E-\left(\overline{H}-E^A_{gs}\right)+i\eta}\overline{a^\dagger_\beta}|\Phi_0\rangle + \langle\Phi_{0,L}|\overline{a^\dagger_\beta}\frac{1}{E-\left(E^A_{gs}-\overline{H}\right)-i\eta}\overline{a_\alpha}|\Phi_0\rangle. \quad (10)$$

In the expression above, $\overline{a_\alpha}=e^{-T}a_\alpha e^T$ and $\overline{a^\dagger_\beta}=e^{-T}a^\dagger_\beta e^T$ are the similarity-transformed annihilation and creation operators, respectively. We note that the truncation of the cluster operator T is reflected in the expression of the coupled-cluster Green's function (10) and, if all excitations up to Ap-Ah were taken into account in the expansion (8), the Green's function (10) would be exact and identical to (1). In principle, the Green's function could be obtained by inserting completeness relations into (10), with the solutions of the $A\pm1$ systems obtained with the particle-attached equation of motion (PA-EOM) and particle-removed equation of motion (PR-EOM) coupled-cluster methods [61]. However, in practice, this approach is difficult to pursue as the sum over all states also involves eigenstates in the continuum. To bypass this issue, we use the Lanczos continued fraction technique [27,32,35,44–46] for the computation of the Green's function Eq. (10).

C. Berggren basis

Our goal is to compute the optical potential for elastic scattering at arbitrary energies. However, as $\eta\to0^+$, the coupled-cluster Green's function in Eq. (10) has poles at energies $E=(E^{A+1}_i-E^A_{gs})$ (with E^{A+1}_i being the eigenvalues of the $A+1$ system), which make the numerical calculation unstable.

In order to bypass this issue, we consider, as we did in Ref. [35], an analytic continuation of the Green's function in the complex-energy plane. This is achieved by working in the complex Berggren basis (generated by the HF potential), which includes bound, resonant, and discretized nonresonant continuum states [47–51]. In our previous work, we considered only NN interactions, while in this work we also consider 3NFs, and the transformation of the Hamiltonian to the Berggren basis is thus much more involved. In order to obtain the Berggren HF basis and transform the Hamiltonian with 3NFs to this basis, we follow the numerically efficient procedure outlined in Ref. [62]. As a consequence, the many-body spectrum for the $A+1$ ($A-1$) systems obtained with the PA-EOM (PR-EOM) is composed of bound, resonant, and complex-continuum states, i.e., the poles of the analytically continued Green's function have either a negative real or complex energy. In that case, the Green's function matrix elements for $E\geqslant0$ smoothly converge to a finite value as $\eta\to0^+$.

In order to fulfill the Berggren completeness [47], the complex-continuum single-particle states must be located along a contour L^+ in the fourth quadrant of the complex momentum plane, below the resonant single-particle states. According to the Cauchy theorem, the form of the contour L^+ is not important, as long as all resonant states lie between the contour and the real momentum axis. The Berggren completeness then reads

$$\sum_i|u_i\rangle\langle\tilde{u_i}|+\int_{L^+}dk|u(k)\rangle\langle\tilde{u(k)}|=\hat{1}, \quad (11)$$

where $|u_i\rangle$ are discrete states corresponding to bound and resonant solutions of the single-particle potential, and $|u(k)\rangle$ are complex-energy scattering states along the complex-contour L^+. In practice, the integral along the complex continuum is discretized, yielding a finite discrete basis set.

III. RESULTS

We present here applications of the coupled-cluster Green's function approach for ^{40}Ca and ^{48}Ca. We show results for the bound states in ^{41}Ca and ^{49}Ca as well as for the neutron elastic scattering.

Calculations are performed using the NNLO$_{\rm sat}$ chiral interaction [52] which reproduces the binding energy and charge radius for both systems [53,54]. All results reported here are obtained from coupled-cluster calculations truncated at the CCSD level, while the PA-EOM and PR-EOM Lanczos vectors have been truncated at the 2p-1h and 1p-2h excitation level, respectively.

We first perform HF calculations in a single-particle basis that employs a mixed representation of harmonic oscillator and Berggren states. More precisely, to calculate a neutron-target optical potential in the (l,j) channel, we use only Berggren states for the (l,j) neutron partial wave, whereas the rest are taken as harmonic oscillator shells. We include all harmonic oscillator shells such that $2n+l\leqslant N_{\rm max}$. We checked that the results do not require a special treatment of the continuum in the other partial waves. The Berggren states are introduced as a discretized set of $N_{\rm berg}=50$ states along a contour in the complex-k plane up to $k_{\rm max}=4$ fm^{-1}. This is sufficiently precise to ensure that results are independent of the form of the contour in the complex plane.

The NNLO$_{\rm sat}$ interaction includes two-body and three-body terms. Let us denote by N_2 and N_3 the cutoffs of the interaction terms defined respectively as the maximum number of quanta allowed in the relative motion of two nucleons and three nucleons. In all calculations here, we always take $N_2=N_{\rm max}$ and N_3 is taken equal to $N_{\rm max}$, except for the most extensive calculations considered here where $N_{\rm max}=14$ and $N_3=16$. Moreover, the three-nucleon forces are truncated at the normal-ordered two-body level in the HF basis [62]. The harmonic oscillator frequency is kept fixed at $\hbar\omega=16$ MeV.

To provide perspective, we also show results for the neutron elastic scattering obtained with the chiral NN interaction NNLO$_{\rm opt}$ interaction [57]. In that case, the calculations were carried out for $N_{\rm max}=14$ with the harmonic oscillator frequency $\hbar\omega=20$ MeV.

We begin by studying the numerical convergence for the bound states and the associated optical potentials in ^{41}Ca and ^{49}Ca.

TABLE I. PA-EOM CCSD energies (in MeV) for bound states in ^{41}Ca and ^{49}Ca calculated with the chiral NNLO$_{sat}$ interaction as a function of N_{max}.

	N_{max}	$E(7/2^-)$	$E(3/2^-)$	$E(1/2^-)$
^{41}Ca				
	12	−7.35	−3.47	−1.31
	14	−7.62	−3.87	−1.80
	14 ($N_3 = 16$)	−7.84	−4.07	−2.15
Exp		−8.36	−6.42	−4.74
^{49}Ca		$E(3/2^-)$	$E(1/2^-)$	$E(5/2^-)$
	12	−3.88	−2.025	−0.37
	14	−4.35	−2.40	−1.00
	14 ($N_3 = 16$)	−4.56	−2.45	−1.42
Exp		−5.14	−3.12	−1.56

A. Convergence for bound states

The energy for the bound states in ^{41}Ca and ^{49}Ca, solutions of the PA-EOM CCSD equations, are shown in Table I as a function of N_{max}. For both nuclei, there are only three bound states supported by the NNLO$_{sat}$ Hamiltonian. As expected, the convergence pattern is slower for the higher energy states. Specifically, for ^{41}Ca, the difference between the energies obtained for $(N_{max}, N_3) = (14,14)$ and $(14,16)$ is ≈220 keV in the case of the ground state, whereas it is ≈350 keV in the case of the $J^\pi = 1/2^-$ second excited state. For ^{49}Ca, the difference is ≈210 keV for the ground state and ≈420 keV for the $J^\pi = 5/2^-$ excited state.

Even though the absolute binding energy is underestimated in the CCSD approximation, when compared to experiment (for ^{40}Ca we obtain a binding energy of 299.28 MeV for $(N_{max}, N_3) = (14, 16)$, whereas the experimental value is 342.05 MeV), the neutron separation energies are consistently within 600 keV of the experimental values. By including both perturbative triple excitations and perturbative estimates for the neglected residual 3NFs (3NF terms beyond the normal-ordered two-body approximation), a good agreement with experimental binding energies can be obtained for ^{40,48}Ca [53].

We show for illustration in Fig. 1, the converging pattern of the real part of the radial (diagonal) optical potential for the three bound states in ^{41}Ca. By construction, the calculated eigenenergies of these potentials are equal to the bound-state energies in Table I when using the effective mass $m\ A/(A-1)$ instead of the actual reduced mass $m\ (A-1)/A$. This can be traced to Eq. (3), where the effective mass associated with the kinetic operator is equal to $m\ A/(A-1)$.

In the following, we study the convergence pattern for the neutron elastic scattering on ^{40}Ca and ^{48}Ca and the corresponding optical potentials.

B. Convergence for scattering states

We now turn our attention to the neutron elastic scattering on ^{40}Ca and ^{48}Ca. For each partial wave, the scattering phase shift is calculated from the single-particle Schrödinger

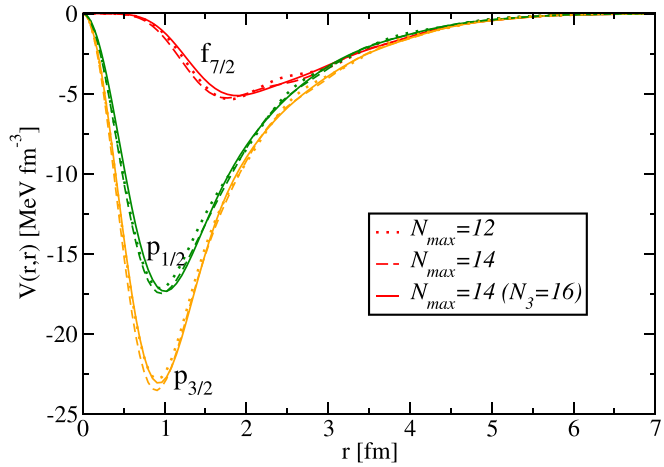

FIG. 1. Real part of the radial (diagonal) optical potential for the bound states in ^{41}Ca, calculated with the NNLO$_{sat}$ interaction. Results are shown for the $f_{7/2}$, $p_{3/2}$, and $p_{1/2}$ neutron partial waves and for several values of N_{max}.

equation using the optical potential in Eq. (6) and the reduced mass $m\ (A-1)/A$. Few comments are in order here. Since the calculations of the optical potential are performed using the laboratory coordinates [the Hamiltonian H in Eq. (3) is defined with these coordinates], the optical potential in Eq. (6) is obtained in these coordinates and not in the relative neutron-target coordinate. However, we will assume here that we can identify the potential in the relative coordinate with the potential calculated with Eq. (6). The error associated with this approximation gets smaller as the mass of the nuclei involved increases [63].

We show in Table II the real part of the phase shifts for a few partial waves for each isotope, at a given scattering beam energy. The results are shown as a function of N_{max} for neutron scattering at $E = 5.17$ MeV on ^{40}Ca, and at $E = 7.81$ MeV on ^{48}Ca. One can see that some of the phase shifts in Table II are well converged, whereas there are variations with the model-space sizes in other cases. For instance, convergence is reached for all but the $s_{1/2}$ and $d_{3/2}$ partial waves for the neutron scattering on ^{40}Ca at 5.17 MeV. For the neutron scattering on ^{48}Ca at 7.81 MeV, the phase

TABLE II. Real part (in degrees) of the neutron scattering phase shifts calculated with the NNLO$_{sat}$ Hamiltonian at 5.17 MeV for ^{40}Ca and 7.81 MeV for ^{48}Ca. Results are shown as a function of N_{max}.

	N_{max}	$\delta_{s_{1/2}}$	$\delta_{p_{1/2}}$	$\delta_{p_{3/2}}$	$\delta_{d_{3/2}}$	$\delta_{d_{5/2}}$
^{40}Ca	($E = 5.17$ MeV)					
	12	−93	80	89	1	−99
	14	−75	77	88	18	−86
	14 ($N_3 = 16$)	−68	78	89	35	−86
		$\delta_{s_{1/2}}$	$\delta_{p_{1/2}}$	$\delta_{p_{3/2}}$	$\delta_{g_{7/2}}$	$\delta_{g_{9/2}}$
^{48}Ca	($E = 7.81$ MeV)					
	12	−93	55	62	13	−10
	14	−83	53	65	22	−10
	14 ($N_3 = 16$)	−85	53	69	37	−11

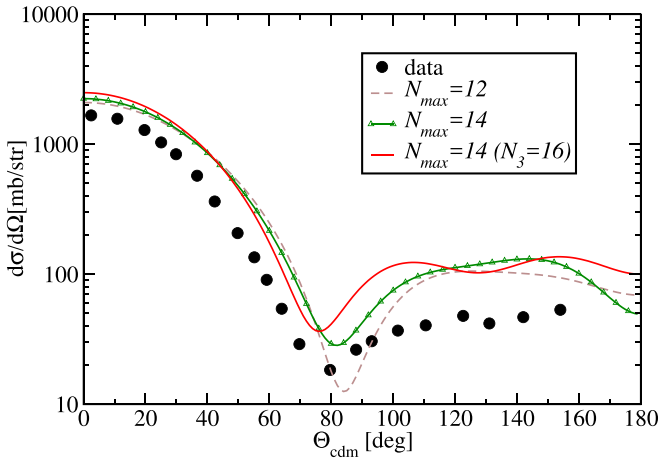

FIG. 2. Differential elastic cross section for ^{40}Ca$(n,n)^{40}$Ca at 5.17 MeV, calculated with the NNLO$_{sat}$ interaction, as a function of N_{max}. Data points are taken from Ref. [58].

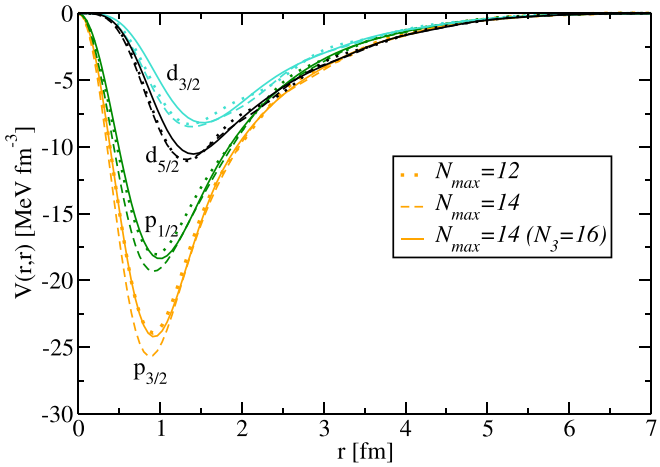

FIG. 4. Real part of the diagonal optical potential for ^{40}Ca$(n,n)^{40}$Ca at $E = 5.17$ MeV, calculated with the NNLO$_{sat}$ interaction, as a function of N_{max}. Results are shown for the neutron $p_{1/2}$, $p_{3/2}$, $d_{3/2}$, $d_{5/2}$ partial waves.

shifts are converged for all but the $g_{7/2}$ partial wave. This difference in the convergence pattern is not unexpected and we have found that the partial waves for which the phase shifts converge slower correspond to those that exhibit a stronger energy dependence around the energy of interest.

For both systems, the phase shifts should have a finite imaginary part which reflects the loss of flux in the elastic channel. For instance, in the case of ^{40}Ca at $E = 5.17$ MeV, there is a potential absorption due to excitation of ^{40}Ca to either its first excited state $E(0^+) = 3.35$ MeV or second excited state $E(3^-) = 3.74$ MeV. However, calculations yield a negligible value for the absorption in all partial waves. We will return to this point in the next section.

Next, we obtain elastic angular distributions by summing the contribution from each partial wave. We show in Figs. 2 and 3 the angular distribution for ^{40}Ca$(n,n)^{40}$Ca at 5.17 MeV and ^{48}Ca$(n,n)^{48}$Ca at 7.81 MeV, as a function of N_{max}. We find that the inclusion of partial waves with angular momentum $L \leqslant 5$ and $L \leqslant 6$ is sufficient for ^{40}Ca and ^{48}Ca, respectively, the contribution of partial waves with higher L being negligible. All scattering phase shifts other than the ones shown in Table II have converged with respect to N_{max}. The variations around the first minimum are significant and are a consequence of the convergence pattern of the scattering phase shifts with N_{max}. We understand then that the calculated cross sections will contain an error due to the model-space truncation. Note that however, for $(N_{max}, N_3) = (14, 16)$, the calculated distribution for ^{48}Ca$(n,n)^{48}$Ca is already in excellent agreement with the data at lower angles where the differential cross section is the largest.

Finally, we show for illustration in Fig. 4, the converging pattern of the real (diagonal) part of the optical potentials in the neutron p, d partial waves for ^{40}Ca$(n,n)^{40}$Ca at 5.17 MeV as a function of N_{max}. All corresponding phase shifts have converged excepted for the $d_{3/2}$ partial wave (cf. Table II).

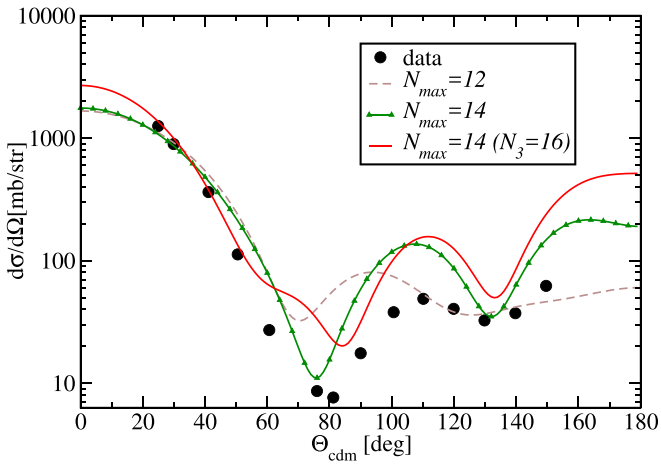

FIG. 3. Differential elastic cross section for ^{48}Ca$(n,n)^{48}$Ca at 7.81 MeV, with the NNLO$_{sat}$ interaction, as a function of N_{max}. Data points are taken from Ref. [58].

C. Results with finite values of η

As we mentioned previously, the calculated optical potentials for neutron scattering on ^{40}Ca at $E = 5.17$ MeV and ^{48}Ca at 7.81 MeV both have negligible absorption.

In order to understand this feature better, let us consider in more detail the scattering on ^{40}Ca at 5.17 MeV. In that case, there is enough energy for the scattered neutron to excite the target (^{40}Ca in its ground state) to its two first excited states located at $E(0^+) = 3.35$ MeV and $E(3^-) = 3.74$ MeV. However, the 0^+ excited state (which is known to have significant 4p-4h components) is not properly captured in the EOM-CCSD approximation: Its calculated energy is at 15.98 MeV above the ground state. On the other hand, the energy of the second excited state is well reproduced at the EOM-CCSD level with $E_{\mathrm{EOM-CCSD}}(3^-) = 3.94$ MeV. Consequently, only potential excitation to the second excited state could in principle be accounted for. The fact that the calculated absorption is nevertheless negligible implies that the CCSD and PA-EOM wave functions are not sufficiently

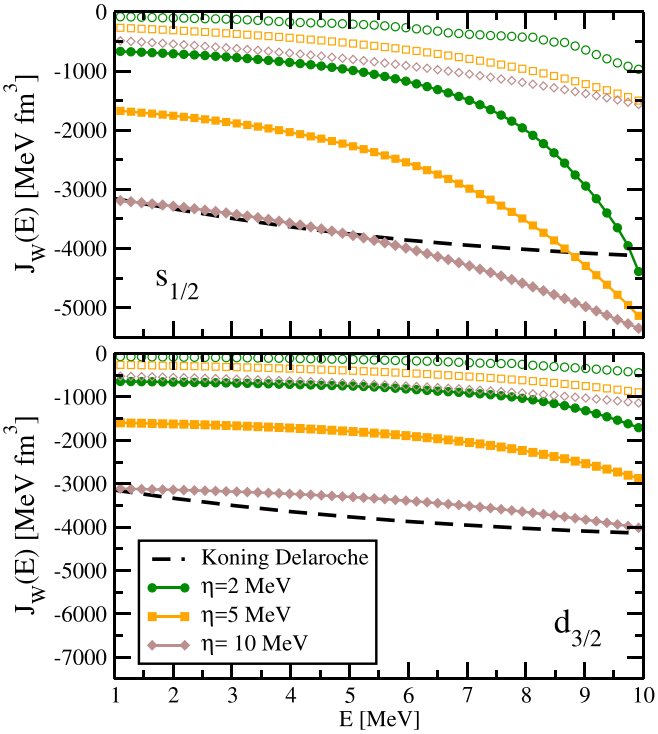

FIG. 5. Volume integral $J_W(E)$ of the imaginary part of the neutron optical potential in the $s_{1/2}$ (upper panel) and $d_{3/2}$ (lower panel) partial wave for ^{40}Ca$(n,n)^{40}$Ca as a function of energy E. Results are shown for the NNLO$_{\rm sat}$ (symbols with lines) and NNLO$_{\rm opt}$ (symbols without lines) interactions at $\eta = 2, 5, 10$ MeV. Results for the KD potential are also shown for comparison.

correlated. In other words, correlations beyond the singles and doubles truncation level are needed to account for the absorption due to target excitation. The situation is similar for the scattering off of ^{48}Ca: In that case, the position of the first excited state $E(2^+) = 3.83$ MeV is fairly well reproduced at the EOM-CCSD level with $E_{\rm EOM-CCSD}(2^+)$ =4.65 MeV, but the calculated absorption is still negligible, pointing out again to a lack of correlations in the CCSD and PA-EOM wave functions.

We should also note that the formation of a compound nucleus will contribute to flux removal from the elastic channel. However, again, at that level of truncation, this cannot be accounted for since the compound states consist of a high number of particle-hole excitations and are usually described by stochastic approaches [64].

We have seen here that one would need to consider excitations beyond the single and double excitations to describe the absorption seen in nature. However, a cheaper solution may be provided by artificially considering finite values of η instead of taking the limit $\eta \to 0^+$ [see Eq. (10)]. In the following, we explore the impact of using finite η values on the optical potential and the scattering phase shift.

We show in Fig. 5 the imaginary volume integral $J_W^l(E)$,

$$J_W^l(E) = 4\pi \int dr r^2 \int dr' r'^2 \mathrm{Im}\Sigma_l'(r, r'; E), \qquad (12)$$

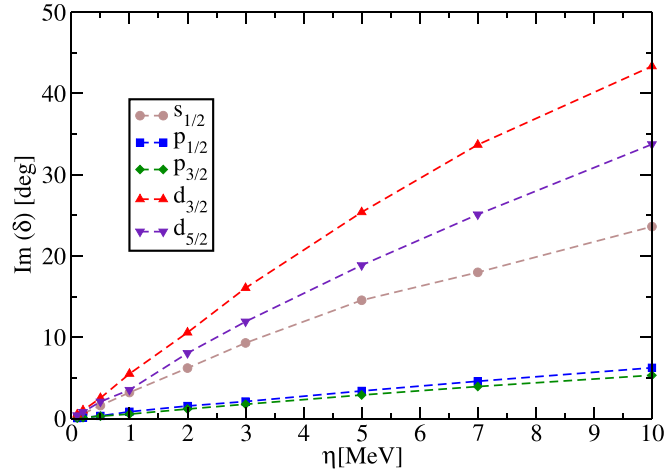

FIG. 6. Imaginary part of the phase shift in the *spd* partial waves for ^{40}Ca$(n,n)^{40}$Ca at 5.17 MeV as a function of η.

of the optical potential for ^{40}Ca$(n,n)^{40}$Ca in the $s_{1/2}$ and $d_{3/2}$ partial waves with $\eta = 2, 5, 10$ MeV. Results are shown for the NNLO$_{\rm sat}$ and NNLO$_{\rm opt}$ interactions and the KD potential. While these quantities are not observables, the comparison with the integral of the KD potential is instructive (see Fig. 5) and underscores the lack of significant absorption of the potential calculated with the coupled-cluster Green's function at the singles and doubles approximation level. Obviously, increasing the value of η increases the value of the integrals

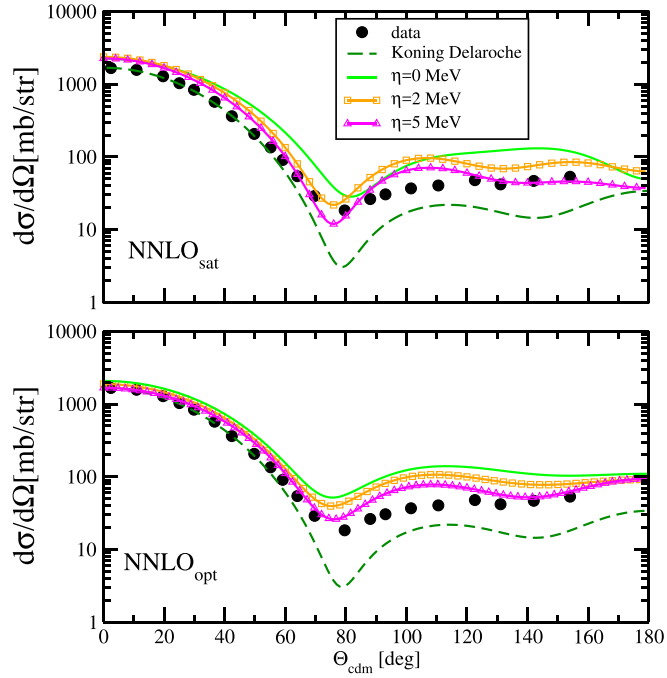

FIG. 7. Differential elastic cross section for ^{40}Ca$(n,n)^{40}$Ca at 5.17 MeV calculated with the NNLO$_{\rm sat}$ (top) and NNLO$_{\rm opt}$ (bottom) interactions. Calculations are shown for $\eta = 0, 2, 5$ MeV. Results obtained using the KD potential are shown for comparison. Data points are taken from Ref. [58].

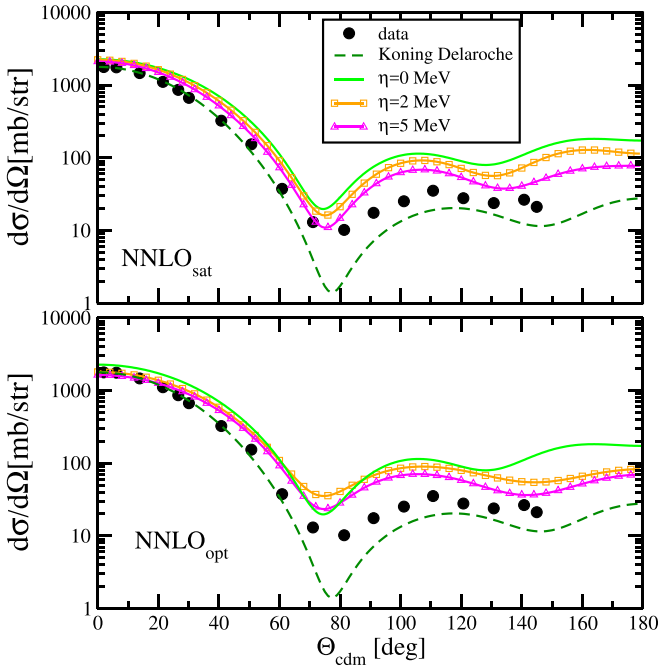

FIG. 8. Differential elastic cross section for ^{40}Ca$(n,n)^{40}$Ca at 6.34 MeV calculated with the NNLO$_{sat}$ (top) and NNLO$_{opt}$ (bottom) interactions. Calculations are shown for $\eta = 0, 2, 5$ MeV. Results obtained using the KD potential are shown for comparison. Data points are taken from Ref. [58].

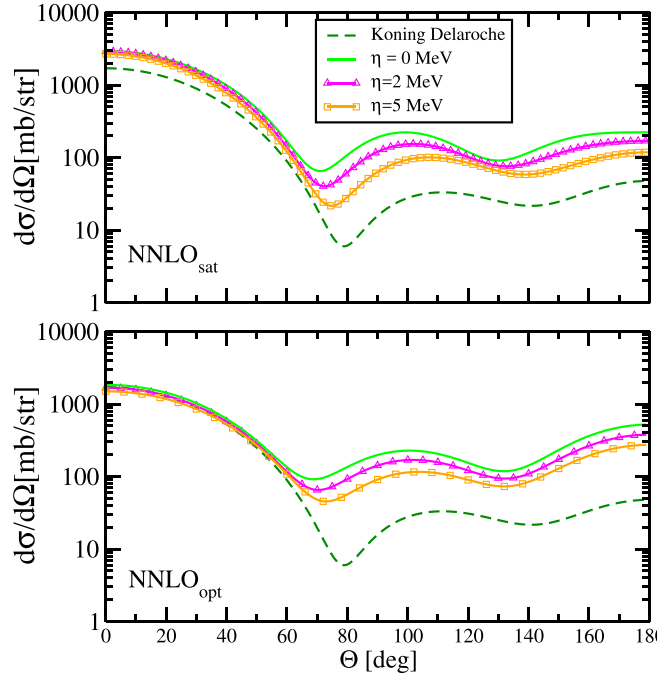

FIG. 9. Differential elastic cross section for ^{48}Ca$(n,n)^{48}$Ca at 4.00 MeV calculated with the NNLO$_{sat}$ (top) and NNLO$_{opt}$ (bottom) interactions. Calculations are shown for $\eta = 0, 2, 5$ MeV. Results obtained using the KD potential are shown for comparison.

(in modulus) and consequently the neutron absorption in the scattering reaction. This is further illustrated in Fig. 6 where we show the imaginary part of the scattering phase shifts for ^{40}Ca$(n,n)^{40}$Ca at 5.17 MeV as a function of η. For $\eta =$ 0 MeV, all phase shifts have a vanishing imaginary part and as η increases, the imaginary parts increase more or less depending on the partial wave considered. If we were interested in reproducing the volume integral of the KD potential at 5.17 MeV in the $s_{1/2}$ partial wave, one would choose a value of $\eta \sim 10$ MeV (see Fig. 5).

In the following section, we show results for the elastic cross section on ^{40}Ca and ^{48}Ca with increasing absorption by using finite values of η.

D. Results for elastic scattering

We now discuss predictions for the elastic cross section when considering values of $\eta = 0, 2, 5$ MeV, for ^{40}Ca and ^{48}Ca. All calculations presented in this section correspond to the largest model space discussed in the previous section namely $N_{\max} = 14$ and $N_3 = 16$.

The calculated differential elastic cross sections for neutron scattering on ^{40}Ca at $E = 5.17$ MeV and $E = 6.4$ MeV are shown in Figs. 7 and 8, respectively. The top (bottom) panel corresponds to the results using the NNLO$_{sat}$ (NNLO$_{opt}$) interaction. For comparison, we also show the angular distributions obtained with the phenomenological KD potential, and also the measured cross sections (errors on the data are smaller than the symbols). As expected, when η increases, the elastic scattering cross section decreases with a more pronounced (relative) reduction at larger angles. Moreover, the agreement with data improves as η increases. The level of disagreement between the experimental data and the result obtained with KD is an illustration of the level of accuracy that can be expected from a phenomenological global interaction.

Next, we show predictions for neutron elastic scattering on ^{48}Ca at $E = 4$ MeV (Fig. 9) and $E = 7.81$ MeV (Fig. 10). There is no data available for the neutron elastic scattering at 4 MeV, but we chose to include it in our study to show that the general behavior of increasing absorption is the same independent of the scattering energy and the target system. As for ^{40}Ca, it is also clear that when including η as a fine-tuning parameter we can improve the agreement with data. Note that even at $\eta = 0$ MeV, the calculated distribution for NNLO$_{sat}$ in Fig. 10 is in excellent agreement with the data at smaller angles where the differential cross section is the largest. The same characteristics shown for ^{40}Ca are present in ^{48}Ca case, namely the cross section is not strongly dependent on η at small angles, while at larger angles the cross section is significantly reduced with increasing η. Moreover, for both nuclei, the results show a sensitivity of the distributions to the employed Hamiltonian.

An encouraging result of our calculations is that, within the energy range considered in this work, fine-tuning η allows us to improve the description of neutron elastic scattering for both ^{40}Ca and ^{48}Ca. The value of η we use should not be interpreted as the effective width of the states, but rather as a means to compensate for the truncations inherent to our approach.

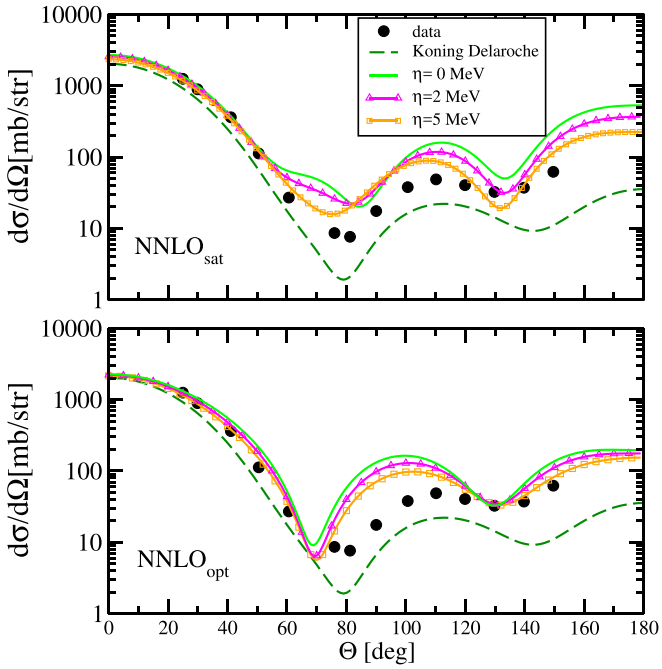

FIG. 10. Differential elastic cross section for ^{48}Ca$(n,n)^{48}$Ca at 7.81 MeV calculated with the NNLO$_{sat}$ (top) and NNLO$_{opt}$ (bottom) interactions. Calculations are shown for $\eta = 0, 2, 5$ MeV. Results obtained using the KD potential are shown for comparison. Data points are taken from Ref. [58].

Finally in Table III, we show the total elastic cross sections for both isotopes and energies, as a function of η. These were obtained by integrating the differential cross sections over angle. We only show the value for NNLO$_{sat}$ (the same features appear when using NNLO$_{opt}$). We also include an error based on the model space truncation: We assign an error as being the difference between the total cross section obtained with $N_{max}, N_3 = (14, 16)$ and that for $(N_{max}, N_3) = (14, 16)$. In the last column, we show the results using the phenomenological interaction KD. In all cases, we can see that the cross sections calculated with the coupled-cluster optical potential are larger than the predictions obtained with the KD potential.

TABLE III. Total elastic cross sections (in b) calculated with the NNLO$_{sat}$ interaction for ^{40}Ca and ^{48}Ca. Results are shown for $\eta = 0, 2, 5$ MeV. For each case, we assign an error defined as the difference between the calculated cross section obtained with $(N_{max}, N_3) = (14, 16)$ and $(N_{max}, N_3) = (14, 14)$. Results obtained with the KD potential are shown for comparison.

A	E (MeV)	$\eta = 0$ MeV	$\eta = 2$ MeV	$\eta = 5$ MeV	KD
40	5.17	229(12)	195(13)	166(12)	108
	6.3	195(3)	169(10)	144(9)	96
48	7.81	182 (32)	159(13)	139 (12)	88

IV. CONCLUSIONS

In this paper, we constructed microscopic nuclear optical potentials by combining the Green's function approach with the coupled-cluster method at the singles and doubles truncation level. We used an analytical continuation in the complex-energy plane, based on a complex Berggren basis, to compute the Green's function. The Dyson equation was then inverted to obtain the optical potential. We showed applications for ^{40}Ca and ^{48}Ca with the chiral NN and 3NF interaction NNLO$_{sat}$. The choice of this interaction was motivated by the fact that it allows for a good description of masses and radii in a wide mass range and furthermore reproduces the charge radii of ^{40}Ca and ^{48}Ca. First, we showed results for the optical potentials associated with the bound states in ^{41}Ca and ^{49}Ca and then presented applications to the neutron scattering. We also showed, for comparison, the results for neutron scattering obtained with the chiral NN interaction NNLO$_{opt}$ and with the phenomenological Koning-Delaroche potential. We have seen that the overall form of the scattering cross section is reproduced for both nuclei at several scattering energies. At this level of truncation, the absorption is practically negligible, which points to a lack of many-body correlations in the wave functions of the coupled-cluster method at the singles and doubles approximation level. We showed that by increasing the parameter η in the Green's function, results can be somewhat improved.

This work can be extended in several directions. We plan to consider higher order correlations in our coupled-cluster Green's function calculations as was recently done for the dipole response of ^{48}Ca [65] and excited states in ^{101}Sn [8]. The first step will be to include iterative triples excitations in the ground state and investigate the impact of these correlations on the absorptive character of the calculated optical potential. It could also be interesting to investigate optical potentials constructed by starting with the singles and doubles coupled-cluster Green's function potential and add an *ad hoc* polarization terms which would effectively account for the missing physics (such as collective excitations and formation of compound nucleus) at that level of truncations.

The Department of Energy will provide public access to these results of federally sponsored research in accordance with the DOE Public Access Plan [66].

ACKNOWLEDGMENTS

This work has been partially supported by U.S. DOE Grant No. DE-FG02-13ER41967. ORNL is managed by UT-Battelle, LLC, under Contract No. DE-AC05-00OR22725 with the U.S. Department of Energy. The U.S. Government retains, and the publisher, by accepting the article for publication, acknowledges that the U.S. Government retains a nonexclusive, paid-up, irrevocable, worldwide license to publish or reproduce the published form of this manuscript or allow others to do so for U.S. Government purposes.

We thank K. Hebeler for providing us with matrix elements in Jacobi coordinates for the NNN interaction at next-to-next-to-leading order. We acknowledge beneficial discussions with

Willem Dickhoff, Charlotte Elster, Heiko Hergert, and Grégory Potel. This work was supported by the National Science Foundation under Grant No. PHY-1403906, the Department of Energy under Contract No. DE-FG52-08NA28552, by the Office of Science, U.S. Department of Energy under Award No. DE-SC0013365, and by the Office of Nuclear Physics, U.S. Department of Energy, under Grants No. DE-SC0008499 (SciDAC-3 NUCLEI) and No. DE-SC0018223 (SciDAC-4 NUCLEI) and the Field Work Proposals No. ERKBP57 and No. ERKBP72 at Oak Ridge National Laboratory (ORNL). An award of computer time was provided by the Institute for Cyber-Enabled Research at Michigan State University. Part of this research used resources of the Oak Ridge Leadership Computing Facility located at ORNL, which is supported by the Office of Science of the Department of Energy under Contract No. DE-AC05-00OR22725.

[1] http://www.nupecc.org/index.php?display=lrp2016/main.
[2] G. Bollen, FRIB: Facility for Rare Isotope Beams, in *International Symposium on Exotic Nuclei*, AIP Conf. Proc. No. 1224 (AIP, New York, 2010), pp. 432–441.
[3] O. Kester and H. Stöcker, *FAIR Project at GSI* (World Scientific, Singapore, 2016).
[4] I. J. Thompson and F. M. Nunes, *Nuclear Reactions for Astrophysics* (Cambridge University Press, Cambridge, UK, 2009).
[5] U. Van Kolck, Effective field theory of nuclear forces, Prog. Part. Nucl. Phys. **43**, 337 (1999).
[6] E. Epelbaum, H.-W. Hammer, and U.-G. Meißner, Modern theory of nuclear forces, Rev. Mod. Phys. **81**, 1773 (2009).
[7] R. Machleidt and D. R. Entem, Chiral effective field theory and nuclear forces, Phys. Rep. **503**, 1 (2011).
[8] T. D. Morris, J. Simonis, S. R. Stroberg, C. Stumpf, G. Hagen, J. D. Holt, G. R. Jansen, T. Papenbrock, R. Roth, and A. Schwenk, Structure of the Lightest Tin Isotopes, Phys. Rev. Lett. **120**, 152503 (2018).
[9] B. Mihaila and J. H. Heisenberg, Microscopic Calculation of the Inclusive Electron Scattering Structure Function in ^{16}O, Phys. Rev. Lett. **84**, 1403 (2000).
[10] D. J. Dean and M. Hjorth-Jensen, Coupled-cluster approach to nuclear physics, Phys. Rev. C **69**, 054320 (2004).
[11] W. H. Dickhoff and C. Barbieri, Self-consistent Green's function method for nuclei and nuclear matter, Prog. Part. Nucl. Phys. **52**, 377 (2004).
[12] G. Hagen, T. Papenbrock, D. J. Dean, and M. Hjorth-Jensen, Medium-Mass Nuclei from Chiral Nucleon-Nucleon Interactions, Phys. Rev. Lett. **101**, 092502 (2008).
[13] G. Hagen, T. Papenbrock, D. J. Dean, and M. Hjorth-Jensen, *Ab initio* coupled-cluster approach to nuclear structure with modern nucleon-nucleon interactions, Phys. Rev. C **82**, 034330 (2010).
[14] K. Tsukiyama, S. K. Bogner, and A. Schwenk, In-Medium Similarity Renormalization Group for Nuclei, Phys. Rev. Lett. **106**, 222502 (2011).
[15] R. Roth, S. Binder, K. Vobig, A. Calci, J. Langhammer, and P. Navrátil, Medium-Mass Nuclei with Normal-Ordered Chiral $NN+3N$ Interactions, Phys. Rev. Lett. **109**, 052501 (2012).
[16] H. Hergert, S. K. Bogner, S. Binder, A. Calci, J. Langhammer, R. Roth, and A. Schwenk, In-medium similarity renormalization group with chiral two-plus three-nucleon interactions, Phys. Rev. C **87**, 034307 (2013).
[17] V. Somà, A. Cipollone, C. Barbieri, P. Navrátil, and T. Duguet, Chiral two- and three-nucleon forces along medium-mass isotope chains, Phys. Rev. C **89**, 061301 (2014).
[18] S. Binder, P. Piecuch, A. Calci, J. Langhammer, P. Navrátil, and R. Roth, Extension of coupled-cluster theory with a noniterative treatment of connected triply excited clusters to three-body Hamiltonians, Phys. Rev. C **88**, 054319 (2013).
[19] T. A. Lähde, E. Epelbaum, H. Krebs, D. Lee, U.-G. Meißner, and G. Rupak, Lattice effective field theory for medium-mass nuclei, Phys. Lett. B **732**, 110 (2014).
[20] K. M. Nollett, S. C. Pieper, R. B. Wiringa, J. Carlson, and G. M. Hale, Quantum Monte Carlo Calculations of Neutron-α Scattering, Phys. Rev. Lett. **99**, 022502 (2007).
[21] S. Quaglioni and P. Navrátil, *Ab initio* Many-Body Calculations of n-^{3}H, n-^{4}He, p-^{3,4}He, and n-^{10}Be scattering, Phys. Rev. Lett. **101**, 092501 (2008).
[22] G. Hupin, J. Langhammer, P. Navrátil, S. Quaglioni, A. Calci, and R. Roth, *Ab initio* many-body calculations of nucleon-^{4}He scattering with three-nucleon forces, Phys. Rev. C **88**, 054622 (2013).
[23] S. Elhatisari, D. Lee, G. Rupak, E. Epelbaum, H. Krebs, T. A. Lähde, T. Luu, and U.-G. Meißner, *Ab initio* α-α scattering, Nature (London) **528**, 111 (2015).
[24] I. A. Mazur, A. M. Shirokov, A. I. Mazur, and J. P. Vary, Description of resonant states in the shell model, Phys. Part. Nucl. **48**, 84 (2017).
[25] P. Navrátil and S. Quaglioni, *Ab initio* Many-Body Calculations of the ^{3}H$(d, n)^4$He and ^{3}He$(d, p)^4$He Fusion Reactions, Phys. Rev. Lett. **108**, 042503 (2012).
[26] D. Gazit, S. Bacca, N. Barnea, W. Leidemann, and G. Orlandini, Photoabsorption on ^{4}He with a Realistic Nuclear Force, Phys. Rev. Lett. **96**, 112301 (2006).
[27] V. D. Efros, W. Leidemann, G. Orlandini, and N. Barnea, The Lorentz integral transform (LIT) method and its applications to perturbation-induced reactions, J. Phys. G: Nucl. Part. Phys. **34**, R459 (2007).
[28] L. Girlanda, A. Kievsky, L. E. Marcucci, S. Pastore, R. Schiavilla, and M. Viviani, Thermal Neutron Captures on d and ^{3}He, Phys. Rev. Lett. **105**, 232502 (2010).
[29] L. E. Marcucci, R. Schiavilla, and M. Viviani, Proton-Proton Weak Capture in Chiral Effective Field Theory, Phys. Rev. Lett. **110**, 192503 (2013).
[30] P. Navratil, S. Quaglioni, G. Hupin, C. Romero-Redondo, and A. Calci, Unified *ab initio* approaches to nuclear structure and reactions, Phys. Scri. **91**, 053002 (2016).
[31] G. Hagen and N. Michel, Elastic proton scattering of medium mass nuclei from coupled-cluster theory, Phys. Rev. C **86**, 021602 (2012).
[32] S. Bacca, N. Barnea, G. Hagen, M. Miorelli, G. Orlandini, and T. Papenbrock, Giant and pigmy dipole resonances in ^{4}He, ^{16,22}O, and ^{40}Ca from chiral nucleon-nucleon interactions, Phys. Rev. C **90**, 064619 (2014).
[33] S. Bacca and S. Pastore, Electromagnetic reactions on light nuclei, J. Phys. G: Nucl. Part. Phys. **41**, 123002 (2014).

[34] A. Idini, C. Barbieri, and P. Navrátil, *Ab initio* optical potentials and nucleon scattering on medium mass nuclei, Acta Phys. Pol. B **48**, 273 (2017).

[35] J. Rotureau, P. Danielewicz, G. Hagen, F. M. Nunes, and T. Papenbrock, Optical potential from first principles, Phys. Rev. C **95**, 024315 (2017).

[36] C. Barbieri and B. K. Jennings, Nucleon-nucleus optical potential in the particle-hole approach, Phys. Rev. C **72**, 014613 (2005).

[37] M. H. Mahzoon, R. J. Charity, W. H. Dickhoff, H. Dussan, and S. J. Waldecker, Forging the Link between Nuclear Reactions and Nuclear Structure, Phys. Rev. Lett. **112**, 162503 (2014).

[38] C. Barbieri and A. Carbone, Self-consistent Green's function approaches, in *An Advanced Course in Computational Nuclear Physics: Bridging the Scales from Quarks to Neutron Stars*, edited by M. Hjorth-Jensen, M. P. Lombardo, and U. van Kolck (Springer, Cham, 2017), pp. 571–644.

[39] H. Kümmel, K. H. Lührmann, and J. G. Zabolitzky, Many-fermion theory in expS- (or coupled cluster) form, Phys. Rep. **36**, 1 (1978).

[40] R. F. Bishop, An overview of coupled cluster theory and its applications in physics, Theor. Chim. Acta **80**, 95 (1991).

[41] R. J. Bartlett and M. Musiał, Coupled-cluster theory in quantum chemistry, Rev. Mod. Phys. **79**, 291 (2007).

[42] S. Binder, J. Langhammer, A. Calci, and R. Roth, *Ab initio* Path to Heavy Nuclei, Phys. Lett. B **736**, 119 (2014).

[43] G. Hagen, T. Papenbrock, M. Hjorth-Jensen, and D. J. Dean, Coupled-cluster computations of atomic nuclei, Rep. Prog. Phys. **77**, 096302 (2014).

[44] E. Dagotto, Correlated electrons in high-temperature superconductors, Rev. Mod. Phys. **66**, 763 (1994).

[45] K. A. Hallberg, Density-matrix algorithm for the calculation of dynamical properties of low-dimensional systems, Phys. Rev. B **52**, R9827 (1995).

[46] W. C. Haxton, K. M. Nollett, and K. M. Zurek, Piecewise moments method: Generalized Lanczos technique for nuclear response surfaces, Phys. Rev. C **72**, 065501 (2005).

[47] T. Berggren, On the use of resonant states in eigenfunction expansions of scattering and reaction amplitudes, Nucl. Phys. A **109**, 265 (1968).

[48] N. Michel, W. Nazarewicz, M. Płoszajczak, and K. Bennaceur, Gamow Shell Model Description of Neutron-Rich Nuclei, Phys. Rev. Lett. **89**, 042502 (2002).

[49] R. Id Betan, R. J. Liotta, N. Sandulescu, and T. Vertse, Two-Particle Resonant States in a Many-Body Mean Field, Phys. Rev. Lett. **89**, 042501 (2002).

[50] G. Hagen, J. S. Vaagen, and M. Hjorth-Jensen, The contour deformation method in momentum space, applied to subatomic physics, J. Phys. A: Math. Gen. **37**, 8991 (2004).

[51] G. Hagen and J. S. Vaagen, Study of resonant structures in a deformed mean field by the contour deformation method in momentum space, Phys. Rev. C **73**, 034321 (2006).

[52] A. Ekström, G. R. Jansen, K. A. Wendt, G. Hagen, T. Papenbrock, B. D. Carlsson, C. Forssén, M. Hjorth-Jensen, P. Navrátil, and W. Nazarewicz, Accurate nuclear radii and binding energies from a chiral interaction, Phys. Rev. C **91**, 051301 (2015).

[53] G. Hagen, A. Ekström, C. Forssén, G. R. Jansen, W. Nazarewicz, T. Papenbrock, K. A. Wendt, S. Bacca, N. Barnea, B. Carlsson, C. Drischler, K. Hebeler, M. Hjorth-Jensen, M. Miorelli, G. Orlandini, A. Schwenk, and J. Simonis, Neutron and weak-charge distributions of the ^{48}Ca nucleus, Nat. Phys. **12**, 186 (2016).

[54] R. F. Garcia Ruiz, M. L. Bissell, K. Blaum, A. Ekström, N. Frömmgen, G. Hagen, M. Hammen, K. Hebeler, J. D. Holt, G. R. Jansen *et al.*, Unexpectedly large charge radii of neutron-rich calcium isotopes, Nat. Phys. **12**, 594 (2016).

[55] V. Lapoux, V. Somà, C. Barbieri, H. Hergert, J. D. Holt, and S. R. Stroberg, Radii and Binding Energies in Oxygen Isotopes: A Challenge for Nuclear Forces, Phys. Rev. Lett. **117**, 052501 (2016).

[56] T. Duguet, V. Somà, S. Lecluse, C. Barbieri, and P. Navrátil, *Ab initio* calculation of the potential bubble nucleus ^{34}Si, Phys. Rev. C **95**, 034319 (2017).

[57] A. Ekström, G. Baardsen, C. Forssén, G. Hagen, M. Hjorth-Jensen, G. R. Jansen, R. Machleidt, W. Nazarewicz, T. Papenbrock, J. Sarich, and S. M. Wild, Optimized Chiral Nucleon-Nucleon Interaction at Next-To-Next-To-Leading Order, Phys. Rev. Lett. **110**, 192502 (2013).

[58] A. J. Koning and J. P. Delaroche, Local and global nucleon optical models from 1 keV to 200 MeV, Nucl. Phys. A **713**, 231 (2003).

[59] F. Capuzzi and C. Mahaux, Projection operator approach to the self-energy, Ann. Phys. **245**, 147 (1996).

[60] W. H. Dickhoff and D. Van Neck, *Many-Body Theory Exposed!* (World Scientific, Singapore, 2007).

[61] J. R. Gour, P. Piecuch, M. Hjorth-Jensen, M. Włoch, and D. J. Dean, Coupled-cluster calculations for valence systems around ^{16}O, Phys. Rev. C **74**, 024310 (2006).

[62] G. Hagen, M. Hjorth-Jensen, G. R. Jansen, and T. Papenbrock, Emergent properties of nuclei from *ab initio* coupled-cluster calculations, Phys. Scr. **91**, 063006 (2016).

[63] R. C. Johnson, Translation invariance and antisymmetry in the theory of the nucleon optical model, Phys. Rev. C **95**, 064610 (2017).

[64] G. E. Mitchell, A. Richter, and H. A. Weidenmüller, Random matrices and chaos in nuclear physics: Nuclear reactions, Rev. Mod. Phys. **82**, 2845 (2010).

[65] M. Miorelli, S. Bacca, G. Hagen, and T. Papenbrock, Computing the dipole polarizability of ^{48}Ca with increased precision, Phys. Rev. C **98**, 014324 (2018).

[66] http://energy.gov/downloads/doe-public-access-plan.